J. Fluid Mech. (1976), *vol.* 73, *part* 1, *pp.* 97–123
Printed in Great Britain

Structural development of gas–liquid mixture flows

By R. A. HERRINGE
M.D. Research Company, North Ryde, New South Wales, Australia
AND M. R. DAVIS
The University of New South Wales, Kensington, New South Wales, Australia

(Received 1 November 1974 and in revised form 10 March 1975)

The paper describes an experimental study of the structure of air–water mixtures flowing vertically. Resistivity probe techniques were applied to measurements of local void properties, including void fraction, gas–phase convection velocity, bubble size distributions and space–time correlation functions. The axial development of flows for six different air–water mixing conditions were examined. Measurements up to 108 diameters from inlet indicated that, while flow patterns for the different mixers may be significantly different initially, the flows tend to develop towards a common structure determined only by the flux rates of the two phases. This was evidenced by the convergence of the void and velocity profiles, and particularly the bubble size distributions, as the flow developed. Estimates of bubble sizes for these more developed conditions, based on a balance of energy between the interfacial structure and the turbulent structure, gave values of diameters which were on average 13 % above experimental values. The void distributions obtained for bubbly flow conditions, after an adequate settling length, appear to be characterized by a local minimum at the centre of the pipe.

1. Introduction

Gas–liquid mixture pipe flows do not exhibit fully developed equilibrium conditions in the manner characteristic of single-phase flows. The expansion of the gas phase associated with the frictional pressure gradient causes a continual acceleration of the mixture, and consequently a continual flow development. For known mean cross-sectional properties at a given axial location, the existence of predictable cross-sectional phase and velocity distributions has not been verified either theoretically or experimentally. Attempts to use single-phase analytical methods to treat two-phase situations have encountered difficulties because additional variables must be considered, in addition to the problems of turbulent motion which are common to both single-phase and two-phase flows. (See Hewitt & Bouré 1973.) These variables include differences in the velocities of the two phases, the distribution of the phases, compressibility of the gas phase, the existence of interfacial and gravitational forces and the detailed interphase boundary structure of the two-phase mixture.

A major factor which complicates the study of the overall behaviour of two-phase flows is the existence of different flow regimes in which there are gross variations of flow structures and which influence the average characteristics of

the flow. Many different classes of flow pattern have been defined in the literature, although each is generally a special case of one of three basic types of flow in which the gas phase may travel as a core inside a liquid annulus (annular flow), the continuous phase may contain finely dispersed bubbles or droplets across the flow (dispersed flow), or between these extremes, where the phases tend to form into large slugs (slug flow). Further, in horizontal flow the transverse gravitational forces lead to flow stratification in which the phases tend to separate, with the gas phase moving to the top of the pipe (stratified flow). Several flow regime classification diagrams have been presented, indicating the occurrence of a flow regime as a function of two variables such as gas and liquid volume flux (Alves 1954), although these are usually based on a visual assessment at the flow. Griffith & Wallis (1961) related flow patterns in terms of two dimensionless variables: the ratio of gas to total volume flow, and a mixture Froude number based on the mean mixture velocity. This approach was modified by Oshinowo & Charles (1974) by the introduction of a dimensional parameter to include viscosity and surface-tension effects. Although they demonstrated some consistency between their proposed flow pattern correlation and experiments from fairly diverse sources, there are still a significant number of discrepancies. The difficulties in obtaining completely general results undoubtedly stem from our lack of understanding of the mechanisms involved in determining the structure of two-phase flows, and these empirical approaches do little to enhance this knowledge, other than to demonstrate that general flow regimes, which are in many cases predictable, do exist. Whether or not more detailed properties of the flow structure, such as void and velocity distributions or bubble sizes, are predictable depends on whether or not any sort of predictable dynamic equilibrium condition occurs in two-phase flows. Very little experimental evidence of the existence of such equilibrium conditions is available. Neal & Bankoff (1963), using resistivity probes to detect phase changes in mercury–nitrogen flow, demonstrated for a pipe flow containing bubbles and slugs of gas that, after the flow had travelled 51·5 diameters from a 150-mesh screen, the size probability distribution of bubbles was essentially the same for different radial positions. However, even this provides little insight into the mechanisms determining bubble size, and it does not establish the existence of an 'equilibrium' situation independent of initial inlet conditions. More generally, investigators have concluded that phase distributions depend largely on inlet conditions. Miller & Mitchie (1970), Malnes (1966) and Nassos (1963), all using resistivity probe measurements, reported cases where void distributions exhibited local maxima away from the tube centre. All of the profiles reported by Malnes were of this type, and they were attributed to the method of air injection into the water, which was through a porous bronze section of the wall. Miller & Mitchie, using a similar method of air–water mixing, reported void profiles of this type, as well as some with a single maximum near the tube centre. The occurrence of either type of profile depended on the void fraction and the flow rates. For the void profiles measured by Nassos, the air was also injected through the wall of a tube and these void profiles also showed local maxima near the walls. To determine the effects of inlet conditions, Nassos inserted a 100-mesh screen into the flow at the mixer exit, and reported that the

shape of the void profiles changed such that a maximum occurred towards the centre. He thus concluded that void profiles depend on inlet conditions.

In order to determine whether some type of fully developed or equilibrium condition does exist after an adequate settling length, measurements of the properties of the structure of air–water mixture flows were made, with resistivity probes. The general aims of the investigation were to develop signal interpretation techniques for the two-state signal from the resistivity probe. This allows measurements of void fractions, velocities and bubble sizes within the flow. With these techniques developed satisfactorily, it was intended that there would be some indication as to whether the flow structure was dependent on inlet conditions alone, or whether a state of development was reached independent of mixing and inlet effects.

2. Experimental technique

Experimental rig

The experiments were designed to study the structure of the flows during upward vertical flow development in a 5·08 cm diameter perspex pipe, with provision for the location of resistivity probes at various axial positions. To determine the effect of inlet conditions on the flow structure, three different air–water mixers were used, each with and without a wire-mesh screen at outlet to create additional turbulence and mixing. In effect, six different inlet conditions were considered.

Two of the air–water mixers are shown schematically in figure 1. The drilled copper mixer was made up of two sections: the air injection section and the screen chamber. One screen, of 60-mesh, 34 swg monel metal wire gauze with a 40·4 % open area, was used at the position indicated in figure 1 (*a*). The second mixer was similar in construction, but included a length of sintered bronze tube of nominally 10 μm size and 33–43 % porosity, in place of the length of drilled copper tube. A third type of mixer, also shown in figure 1, consisted of three parts: a multijet end-plate, a constant area mixing section and a converging nozzle. When the screen was used with this mixer, it was housed in an additional flange located at the nozzle outlet.

Void fluctuation measurements

A study of various phase detection techniques by Herringe (1973) and Herringe & Davis (1974) indicated that the most suitable method for measuring local instantaneous phase changes in an air–water system of this type is the resistivity probe technique. The use of commonly known γ-ray methods permits the determination only of average values of void fraction. Where resistivity probes are inserted into the flow, an indication of the presence of either phase relies on the change of electrical resistance between two electrodes, when one or both are surrounded by the gas phase. The most suitable probe proved to be a needle probe, where one electrode is the exposed tip of an otherwise insulated needle and the return electrode is the supporting tube. For added versatility, to allow simultaneous measurements at two locations in the flow, a double probe of the type shown in figure 2 was used for the majority of the experiments reported here, so

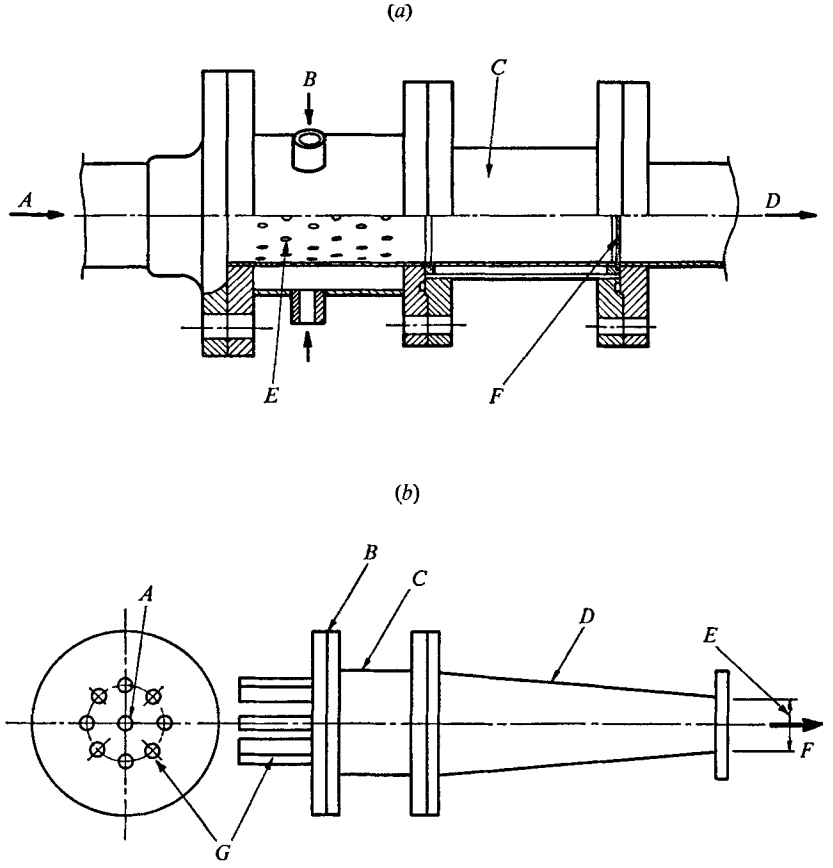

FIGURE 1. Air–water mixers. (*a*) Drilled copper mixer. *A*, Water supply. *B*, Air supply. *C*, Screen chamber. *D*, Two-phase mixture. *E*, 72 holes. *F*, 60-mesh monel screen. (*b*) Nozzle mixer. *A*, Air supply. *B*, Multi-jet end-plate. *C*, Mixing section. *D*, Nozzle. *E*, 5·08 cm I.D. *F*, Two-phase mixture. *G*, Eight injection tubes for water supply.

that simultaneous records of void fluctuations at two axial locations could be analysed. When the tip of one of the needles was in the water phase, the resistance between the needle and the casing was small compared with the value when a bubble surrounded the tip. The change of resistance of each of the needles was detected by the system shown in figure 3. The presence of either phase at the needle tip was indicated by a two-state signal from the Schmidt trigger. This signal was then passed to a counter for determination of bubble frequencies, to an instrument for conversion to a pulse height modulated signal for further analysis by a Hewlett–Packard Correlator/Probability Analyser in probability analysis mode (to determine size distributions), or directly to the Correlator/Probability Analyser in probability mode (to determine void fraction) or in correlation mode (to determine correlation functions).

The detailed tip geometry of the needle probes was found to be critical. Stainless-steel needles with a 0·008 mm tip radius were selected from supplied batches of needles, and epoxy insulation was applied to the entire needle, and allowed to run back whilst drying, to expose only a small tip area. Subsequently

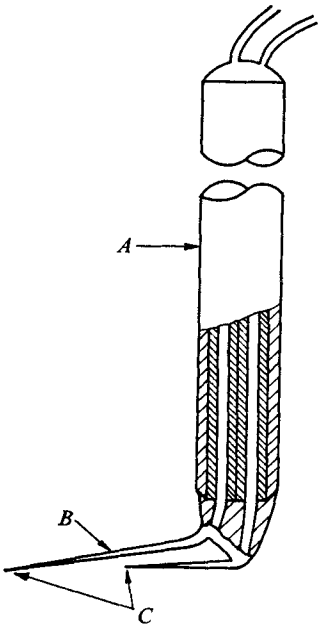

FIGURE 2. Details of resistivity probe for simultaneous void and velocity measurement. Needles were stainless-steel surgical needles, chosen so that tip radius was less than 8 μm. *A*, Stainless-steel tube. *B*, Insulated needles. *C*, Exposed tips.

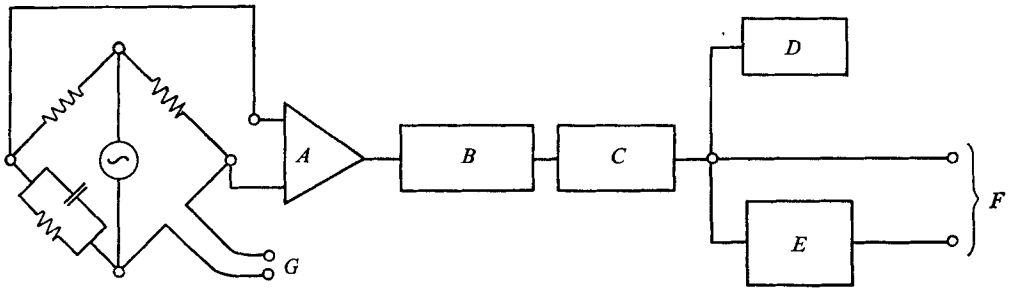

FIGURE 3. Block diagram of resistivity probe signal analysis system. *A*, Amp. *B*, Demodulator. *C*, Schmidt trigger. *D*, Counter. *E*, Pulse height converter. *F*, To correlator/probability analyser. *G*, Probe.

the probes were again selected from the constructed batch on the basis of their performance. It was found that the best performance obtainable corresponded to the satisfactory detection of a bubble of 0·1 mm diameter (i.e. around ten times the tip radius) at a speed of approximately 5 m s^{-1}. The performance was somewhat better at high flow speeds, suggesting that the piercing action of the probe was then more effective. It is likely that the second needle was influenced by the wake of the first, and it generally indicated a rather lower void fraction, suggesting that some bubbles were deflected. However, the second needle was used only to determine flow velocity in the majority of the measurements of profiles across the flow. Correlation measurements, as discussed later in § 5, also suggested some

interference. Since overall budgets of total gas volume flux were found to be balanced by integrating the product of void fraction and velocity over the flow cross-section, it appears that the bubbles smaller than the size resolved by the front needles were very small in number. (This was also borne out by the probability distributions discussed in § 5.) Also, it would appear that the velocity measurements by cross-correlation of the probe signals were not greatly affected.

3. Signal interpretation

Single-point measurements

The response signal from the resistivity probe system consisted of the two-state signal indicating the presence of gas or liquid at the probe tip, which can be defined in terms of a binary variable $\delta(\mathbf{R}, t)$, a function of both position within a flow and time. Thus $\delta(\mathbf{R}, t) = 1$ when the probe tip is instantaneously in the gas phase and $\delta(\mathbf{R}, t) = 0$ in the liquid phase. The local void fraction is here defined as the probability that a point is in the gas phase. For a steady flow the time average void fraction is given by the time average of $\delta(\mathbf{R}, t)$ as

$$\alpha = \lim_{T \to \infty} \frac{1}{T} \int_{-\frac{1}{2}T}^{\frac{1}{2}T} \delta(\mathbf{R}, t)\, dt. \tag{1}$$

The cross-sectional area average void fraction then follows from integration of the void distribution over the area.

The time that the probe tip is in the gas phase (Δt_i) can be used to determine bubble size if the bubble convection velocities (u_c) are known, since the length of the measured chord, x, of a detected bubble is given by

$$x = u_c \Delta t_i. \tag{2}$$

By relating the measured chord lengths to bubble sizes, the void fluctuation measurements can be used to determine these bubble sizes. A relationship of this nature may be derived if it is assumed that all detected bubbles are spherical, and move in the same direction with a common velocity u_c. It is necessary to assume also that the detection probe is negligibly small, and does not deflect bubbles in any way. Provided the flow is locally homogeneous, the probe has equal probability of piercing any point on the projected frontal area and the measured chord length x may vary from zero to the bubble diameter. Further, the diameter of a detected bubble may be between the measured chord length x and infinity.

The above assumptions restrict the application of the analysis to bubbly or dispersed flow situations, because these are the cases for which the mean shape of bubbles may reasonably be assumed to be spherical. The use of a more complicated bubble shape (such as an ellipsoid) in the analysis at this stage seems unwarranted, as such detailed knowledge of the bubble shapes in these turbulent situations is lacking. The formulation of such an analysis would require the assumption of additional parameters, such as the ratio of axes of the ellipsoid. At present it appears preferable to avoid introducing further assumptions with little basis for their detailed formulation. As will be seen in § 5, the similarity of lateral and longitudinal correlations indicates this assumption to be acceptable

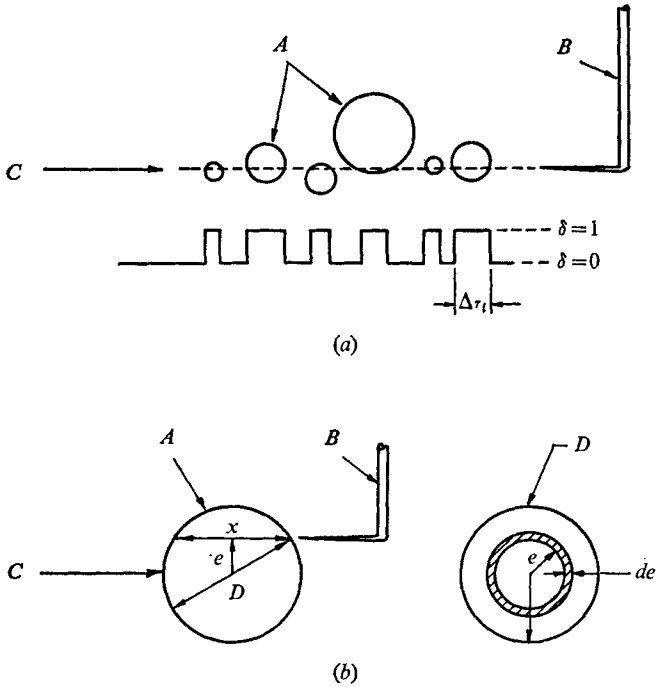

FIGURE 4. Bubble detection by resistivity probe. (*a*) Relation between detected bubbles and response signal. *A*, Bubbles. *B*, Probe. *C*, Flow velocity u_c. (*b*) Relation between measured chord length and bubble diameter. *A*, Spherical bubble of diameter *D*. *B*, Probe. *C*, Flow direction. *D*, Frontal projection.

for the type of well-mixed bubbly flows studied here. This would not be the case for flows with slugs of gas. The assumption of local homogeneity and of a single bubble convection velocity u_c may become less valid as the measuring point approaches the pipe wall, where the size of the bubbles would generally be related to the wall distance, and where a strong shear would exist. The assumption of idealized probe response depends on the construction of the detection probe, and will be valid if the probe tip is very much smaller than the bubbles being detected. For these experiments, the tip radius of the probes was less than 8 μm as previously mentioned.

In general, a bubble detected by the probe tip will not be pierced along a diameter, so that the probe may not pass through the centre of the assumed sphere. Thus, a chord at an eccentricity e is measured, as indicated in figures 4(*a*), (*b*). Under the assumptions discussed above, the probability that the bubble will be pierced along a chord with an eccentricity between e and $e+de$ is given on the basis of the projected frontal areas by

$$\Pr\{e, e+de\} = \frac{2\pi e\, de}{\frac{1}{4}\pi D^2} = \frac{8e}{D^2} de. \tag{3}$$

If the probability density function of the eccentricities of bubble detection for bubbles of a given diameter D is $\rho_1(e/D)$, then we can also write

$$\Pr\{e, e+de\} = \rho_1(e/D)\, de, \tag{4}$$

so that combining (3) and (4) gives

$$\rho_1(e/D) = 8e/D^2. \tag{5}$$

The relation between eccentricity and chord length x is obtained from elementary geometry as

$$x = 2[(\tfrac{1}{2}D)^2 - e^2]^{\frac{1}{2}}. \tag{6}$$

Also, it follows that

$$\Pr\{e, e+de\} = \Pr\{x, x-dx\}, \tag{7}$$

where e and x are related by (6). If we introduce the probability density function of the measured chord lengths for a given bubble diameter D as $\rho_2(x/D)$, then (7) may be rewritten as

$$\rho_1(e/D)\,de = -\rho_2(x/D)\,dx, \tag{8}$$

and obtaining the differential from (6) leads to

$$\rho_2(x/D) = 2x/D^2. \tag{9}$$

The following distribution functions are now introduced: $\rho_3(x)$ as the probability density function of all measured chord lengths for all sizes of bubbles; $\rho_4(D, x)$ as the joint distribution of bubble diameters and chord lengths; and $\rho_5(D)$ as the distribution function of the diameters of all detected bubbles. Thus, the following relations are true:

$$\rho_3(x) = \int_x^\infty \rho_4(D, x)\,dD \tag{10}$$

and

$$\rho_4(D, x) = \rho_2(x/D)\,\rho_5(D). \tag{11}$$

Therefore, from (9)–(11),

$$\frac{\rho_3(x)}{x} = \int_x^\infty \frac{2}{D^2}\rho_5(D)\,dD. \tag{12}$$

This gives

$$\rho_5(x) = \tfrac{1}{2}\{\rho_3(x) - x\rho_3'(x)\}. \tag{13}$$

Equation (13) is the relation between the probability density function of the diameters of all detected bubbles and that of the respective measured chord lengths, with the assumptions previously discussed. Use of (13) to obtain the distribution $\rho_5(x)$ requires differentiation of an experimentally determined curve $\rho_3(x)$, and this operation will magnify any scatter that may be present in the original curve. This effect can be overcome by considering the cumulative probability distribution function which results from $\rho_5(x)$, and which is given after re-arrangement from (13) by

$$P_5(x) = \int_0^x \rho_3(x)\,dx - \tfrac{1}{2}x\rho_3(x). \tag{14}$$

With this last relation, the cumulative probability distribution function of the diameters of all detected bubbles can be obtained from the chord length distributions without any need for differentiation.

The probability density $\rho_5(x)$ represents the distribution of the diameters of bubbles detected by the probe tip; but the question now arises as to whether or not $\rho_5(x)$ (or $P_5(x)$) is the best representation of the physical flow. For a given

flux of bubbles per unit area of flow, there is a greater probability that the probe will detect a large bubble than it will a small one, in proportion to the projected area of the bubble. Thus, in the measured distribution function and consequently in $\rho_5(x)$, the probabilities in the distribution functions are weighted proportionally to D^2. The exact weighting can be determined from the following analysis.

Take a unit cross-sectional flow area with a flux of n bubbles per second, which have diameters between D and $D+dD$, and whose centres pass through the unit cross-section. Then the number of bubbles n_d within this range that are detected per second is

$$n_d = \tfrac{1}{4}\pi D^2, \quad n = \rho_5(D)\,dD\,N_d. \tag{15}$$

We deduce this from the definition of $\rho_5(D)$; and we assume that the n bubbles are uniformly distributed across the unit area section, and that n is sufficiently large for (15) to be statistically significant. N_d is the total rate of bubble detection.

Define a new distribution function $\rho(D)$, which is the probability density function for the diameters of all bubbles with centres passing through a unit area of cross-section. Then the total number of bubbles with diameters between D and $D+dD$ passing through this unit area can be written as

$$n = \rho(D)\,dD\,N. \tag{16}$$

Combining (15) and (16) gives

$$\rho(D) = c[\rho_5(D)/D^2]. \tag{17}$$

$c = 4N_d/(\pi N)$, and the constant c (thus the total bubble flux N) can be determined by normalizing the distribution $\rho(D)$ by letting

$$\int_0^\infty \rho(D)\,dD = 1.$$

The corresponding cumulative distribution function now follows from (17) and (12):

$$P(D) = 1 - c(\rho_3(D)/D). \tag{18}$$

This can be calculated directly from the experimentally measured distribution $\rho_3(D)$, if the constant c is known.

The distributions $\rho(D)$ and $P(D)$ represent the diameters of all bubbles whose centres pass through a unit cross-sectional area of the flow. They are perhaps more representative of the flow situation than $\rho_5(D)$ and $P_5(D)$, which relate to the detected bubbles only. They give a true indication of the number flux density of bubbles within any size range.

Another form of the bubble diameter distribution functions, that has an obvious physical interpretation, is the distribution $\rho_6(D)$. It is defined in terms of the proportionate contribution density to total voidage. The contribution to the total gas volume flow per unit area (dq_g) of bubbles with diameters between D and $D+dD$ is

$$dq_g = n\tfrac{1}{6}\pi D^3 = N\rho(D)\,dD\tfrac{1}{6}\pi D^3 = \rho_6(D)\,dD\,q_g. \tag{19}$$

q_g is the local gas volumetric flux. Thus,

$$\rho_6(D) = \frac{N\pi D^3}{6q_g}, \quad \rho(D) = \frac{2N_d}{3q_g} D\rho_5(D). \tag{20}$$

This distribution $\rho_6(D)$ must be normalized to give unit value for the integral of $\rho_6(D)$. It follows that

$$\frac{3q_g}{2N_d} = \int_0^\infty D\rho_5(D)\,dD. \tag{21}$$

This can be further used to give an estimate of the local volumetric flux q_g once the bubble detection rate has been determined independently. This distribution $\rho_6(D)$ will indicate the relative importance of a given size range of bubbles in determining the overall volumetric gas flow, and hence the local volumetric void fraction. It could also be used, for example, to estimate the effect on void-fraction values of not detecting bubbles too small for a particular void-detection method.

With the foregoing analysis it is possible to determine distributions of the size of bubbles from the probability density function of the chord lengths of detected bubbles, which comes directly from an analysis of the void fluctuation signal. From this chord-length distribution function, we can determine distribution functions representing the diameters of detected bubbles, the diameters of all bubbles passing through a unit cross-section, and the proportionate contribution density to total volumetric voidage from bubbles in a given size range.

The relative merits of using any of these distributions to describe the flow depends on the purpose for which the results are to be used. The simplest distribution to obtain from experimental measurements would be the cumulative distribution function of the diameters of detected bubbles $P_5(D)$ since, given that the distribution of chord lengths is known experimentally, it can be determined without differentiation of the experimental curve. In assessing probe performance, this distribution of detected bubbles would be of interest; the distribution of total bubble flux numbers might be more relevant in considering the kinematic structure of two-phase flows.

4. Space and time correlations

Favre (1965), Champagne, Harris & Corrsin (1970) and Comte-Bellot & Corrsin (1971), amongst others, extended ideas introduced by Taylor (1938) for turbulent single phase flow, and defined a single correlation coefficient, which is a function of both space and time. In a similar manner, we can define for two-phase flows a normalized Eulerian space–time correlation function of the response signal of two probes separated by a distance vector $\mathbf{r}$:

$$R(\mathbf{r},\tau) = \overline{\delta(\mathbf{R},t)\,\delta(\mathbf{R}+\mathbf{r},t+\tau)}\,\{[\overline{\delta(\mathbf{R},t)^2}]^{\frac{1}{2}}\,[\overline{\delta(\mathbf{R}+\mathbf{r},t+\tau)^2}]^{\frac{1}{2}}\}^{-1}. \tag{22}$$

The overbar is used to represent a time averaging process over a long enough period for the function $R(\mathbf{r},\tau)$ to be steady. Of particular interest are cases for which the position vector $\mathbf{r}$ is either perpendicular or parallel to the mean motion of the flow: these will be referred to as lateral and longitudinal correlations, respectively.

From turbulence measurements, the longitudinal correlation coefficient of

velocity fluctuations for a given separation, when presented as a function of time, reaches a maximum for a time delay equal to the mean material transport time between the two measuring points (Favre 1965). In two-phase flow, the time delay τ that gives this maximum correlation can thus be used to determine a mean velocity u_c of the discontinuous phase by the relation $u_c = x/\tau$. (x is the probe separation.) The maximum correlation coefficient will be a decreasing function of probe separation owing to turbulent changes in the bubble structure. The corresponding function for turbulence measurements (of velocity fluctuations) is often integrated with respect to time delay, to obtain an integral time scale which is interpreted as a measure of the structural lifetime of the flow (Champagne *et al.* 1970).

Correlation measurements in turbulence have also been used to describe length scales by integration of the statistical function with zero time delay. This integral length scale was interpreted by Champagne *et al.* (1970) as a measure of the 'spatial large-structure' of the turbulent flow. They further compared this function in the longitudinal direction with the autocorrelation measurement from a single probe, which is the correlation function $R(0,\tau)$, and showed that by using the transformation $\tau = r/u_c$ the two functions are nearly equal.

For the two-state signal $\delta(\mathbf{r},t)$ under consideration in this work, a length scale can be defined by multiplying the convection velocity by the integral time scale; this would be related to both the pulse duration, or measured chord length, and the spacing between pulses. Amiantov & Tikhinov (1965) derived the relation between the autocorrelation function of a random pulse sequence, for which the pulses appeared randomly and were of random duration, with the probability distributions of the pulse durations and the spacing between pulses. They showed that the autocorrelation function can be derived from knowledge of these two probability distributions. However, the derivation of the probability distribution function of the pulse durations from the autocorrelation function can be performed only if the correlation between pulses can be neglected. Under this condition, the probability distribution function of the duration of pulses

$$p(\tau) = \bar{\tau} R''(0,\tau). \tag{23}$$

$R''(0,\tau)$ is the second derivative of the autocorrelation function with respect to τ; and $\bar{\tau}$ is defined by

$$\bar{\tau} = \int_0^\infty \tau p(\tau)\, d\tau. \tag{24}$$

After calculating $p(\tau)$ from (23), where $p(\tau)$ is equivalent to the distribution $\rho_3(x)$ after the transformation $x = u_c\tau$, distribution functions can be calculated by the methods previously outlined in (13) and (14).

By defining a space–time correlation function analogous to that defined for single-phase turbulence measurements, the structure of two-phase flow can be investigated using similar principles to those employed for single-phase turbulence. The moving-axis autocorrelation function can be used to provide a measure of the structural lifetime of the flow, and comparison of lateral and longitudinal spatial correlation functions can be used as an indication of the homogeneity of

Flow condition	Air flow rate ($kg\ s^{-1} \times 10^3$)	Water flow rate ($kg\ s^{-1}$)	Volume flux at 36*D* section: Water ($m\ s^{-1}$)	Volume flux at 36*D* section: Air ($m\ s^{-1}$)
1	0·57	3·80	1·88	0·18
2	1·27	3·80	1·88	0·41
3	2·68	3·80	1·88	0·87
4	2·68	8·46	4·19	0·76
5	3·44	8·46	4·19	0·86
6	10·45	8·46	4·19	2·36
7	4·15	12·05	6·13	0·92
8	7·40	12·05	6·13	1·47
9	17·00	12·05	6·13	3·01

TABLE 1. Standard flow conditions for studies of flow structure in 5·08 cm pipe

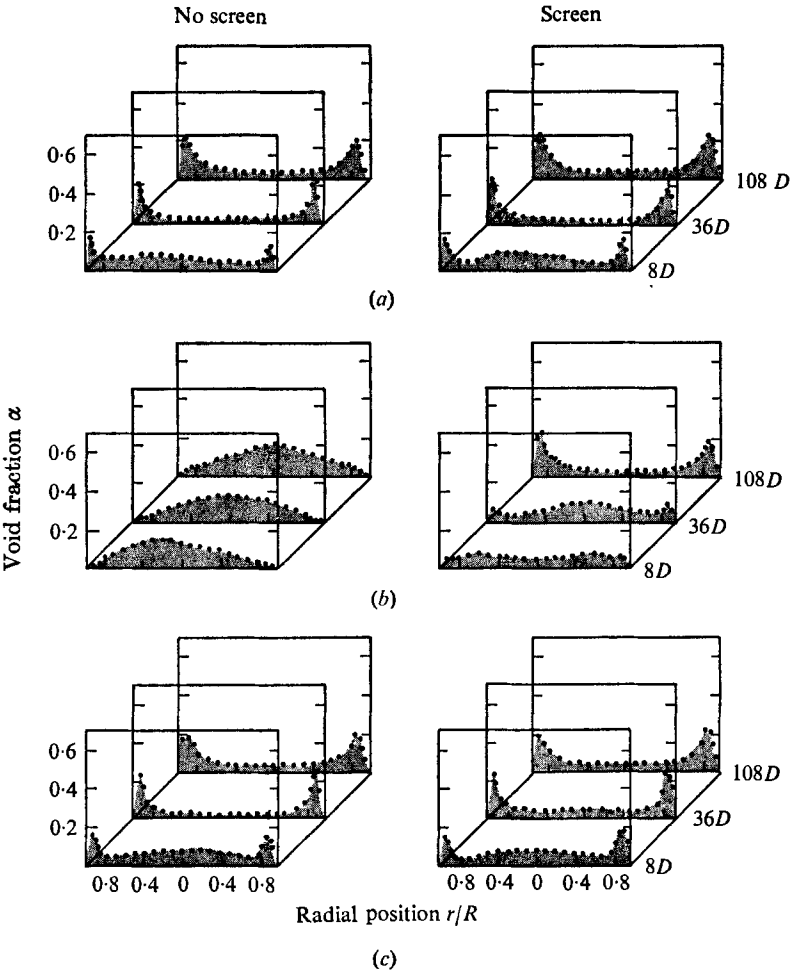

FIGURE 5. Axial development of void profiles. Flow condition 1, $M_g = 5{\cdot}7 \times 10^{-4}\ kg\ s^{-1}$, $M_l = 3{\cdot}80\ kg\ s^{-1}$. Mixers: (*a*) porous bronze; (*b*) drilled copper, (*c*) nozzle.

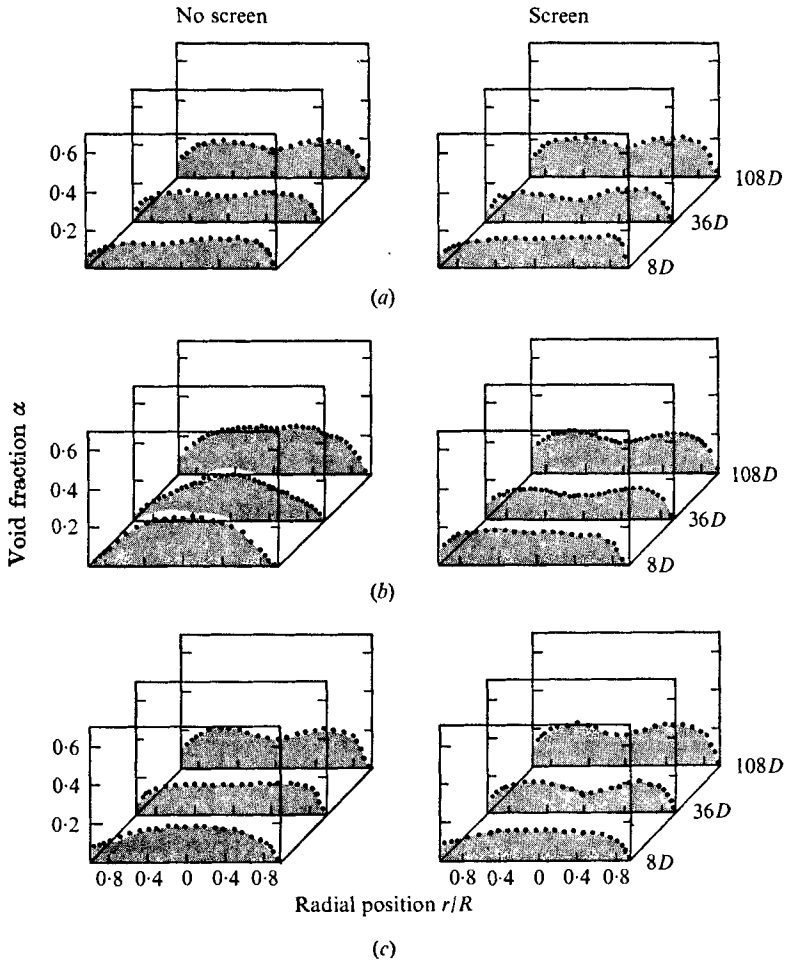

FIGURE 6. Axial development of void profiles. Flow condition 4, $M_g = 2{\cdot}68 \times 10^{-3}$ kg s^{-1}, $M_l = 8{\cdot}46$ kg s^{-1}. Mixers: (*a*) porous bronze, (*b*) drilled copper, (*c*) nozzle.

the flow. Further, when discussing length scales for two-phase flows, a more direct physical interpretation is available, and the autocorrelation function can be related to the bubble size distribution functions directly.

5. Experimental results

Void profiles

As a general indicator of the changing structure during flow development, radial void profiles were determined at 8, 36 and 108 diameters from the inlet, for nine standard flow conditions and for six inlet conditions. The data corresponding to these standard flow conditions are listed in table 1. The complete void profile results for three of the flow conditions are presented in figures 5–7, where we can see that at 8 diameters from inlet the phase distributions are strongly dependent on the type of mixing. This is especially obvious for flow condition 1 in figure 5

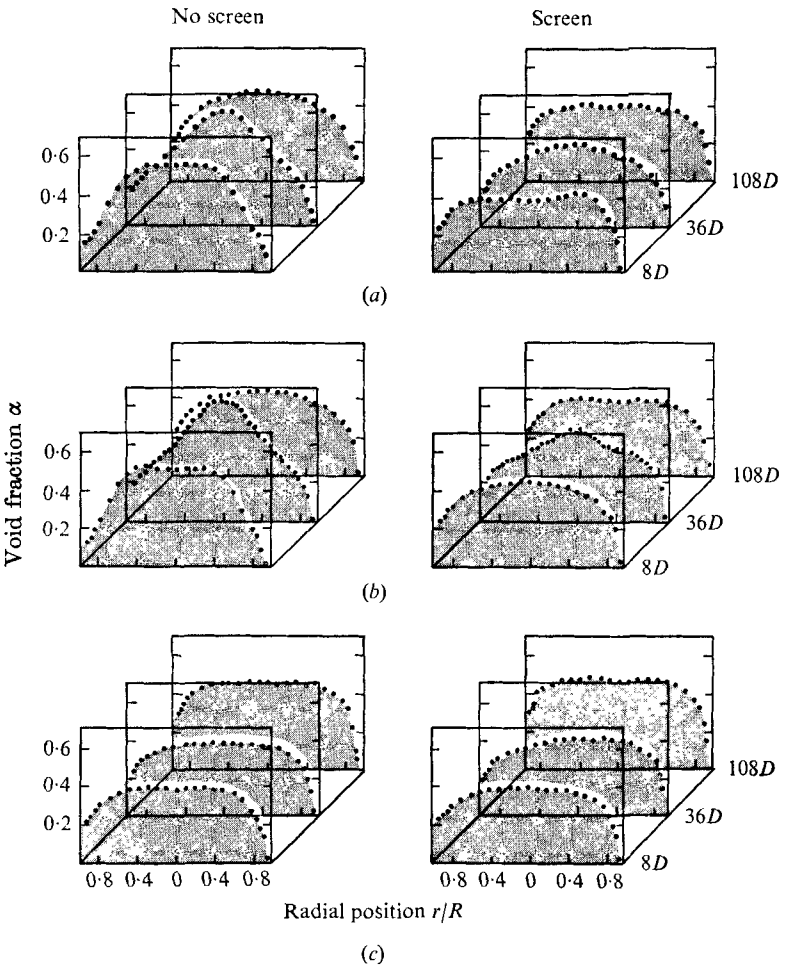

FIGURE 7. Axial development of void profiles. Flow condition 9, $M_g = 1{\cdot}7 \times 10^{-2}$ kg s^{-1}, $M_l = 1{\cdot}21 \times 10$ kg s^{-1}. Mixers: (*a*) porous bronze, (*b*) drilled copper, (c) nozzle.

since at $8D$ the void profile shape for flow from the drilled copper mixer, both with and without the mixing screen, was entirely different from the other mixing conditions. As the flows developed, however, the flow from the drilled copper mixer with the screen developed into the same pattern as the others. For flow condition 4 in figure 6, significant differences occurred between the various void profiles at $8D$; but, as the flow developed, the distributions became essentially the same, except perhaps for the flow from the drilled copper mixer, although this appeared to be approaching the same phase distribution as for the other inlet conditions. Similarly, in figure 7, initial differences in the phase distributions had virtually disappeared by $108D$. These results are typical of those for all the nine flow conditions, where void profile shapes appeared to be relatively unaffected by inlet conditions for flow 108 diameters downstream from inlet. This was especially true for conditions 7 and 8, which appeared to be homogeneous, well-mixed flows at $108D$ with identical void profile shapes for all inlet conditions.

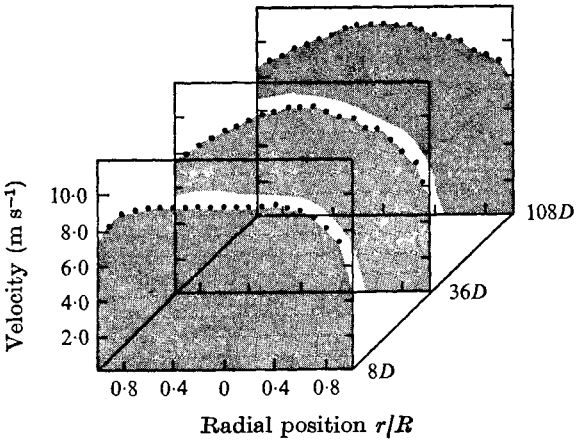

FIGURE 8. Velocity profiles for flow development from drilled copper mixer. Flow condition 9.

Having obtained these results, more detailed flow measurements were made for selected configurations and flow conditions only.

Velocity profiles

Correlation measurements were obtained to determine cross-sectional convection velocity u_c distributions during the axial development of five different flows. The results for one flow from the drilled copper mixer are presented in figure 8. The figure shows that changes in the velocity profile shape are very small compared with changes in the void profiles during flow development, which are presented in figure 7. In order to quantify the changes of shape, and to provide a simple comparison with single-phase results, the measured curves were fitted by a least-squares regression to an empirical equation of the form

$$u_c = a(1 - r/R)^{1/m}. \tag{25}$$

The different values of the constant m thus provide a simple means of comparing the shapes. The constants from (25) are tabulated in table 2: we can see that, for conditions 1 and 2, the profiles for the nozzle mixer are noticeably flatter than those for the drilled copper mixer. This can again be related to the mixer effects, since the differences in velocity profile shapes caused by mixer effects tended to become less obvious as the flow reached $108D$, where the power-law indices were grouped about a $\frac{1}{7}$th power law.

Velocity profiles similar to those in figure 8 were reported for air–water flows by Lackmé (1967), who also used cross-correlation to determine convection velocities. His results for a 32 mm diameter pipe were taken 37·5 diameters downstream from the air–water mixer, which was similar to the drilled copper mixer of this work, with 100 holes of 0·5 mm diameter. The measured velocity profiles were generally much flatter than a $\frac{1}{7}$th power law. Similarly, the velocity profiles measured by Malnes (1966), for vertical steam–water flows in an 80 mm pipe, were flatter than the single-phase profiles. Lecroart & Porte (1971) presented a single velocity distribution as a preliminary result of their resistance

Axial position	Flow condition	Regression constants a nozzle	a d.c.	m nozzle	m d.c.	Average velocity (m s^{-1}) $\langle \alpha U_g \rangle / \langle \alpha \rangle$ nozzle	$\langle \alpha U_g \rangle / \langle \alpha \rangle$ d.c.	$Q_g / A\langle \alpha \rangle$ nozzle	$Q_g / A\langle \alpha \rangle$ d.c.
8D	1	2·58	2·65	7·2	8·6	2·15	2·45	2·27	2·52
	2	2·74	2·90	9·5	7·7	2·36	2·65	2·41	2·73
	4	5·32	5·53	12·9	9 3	4·92	5·10	5·28	5·61
	6	7·09	7·48	8·5	6·6	6·31	6·68	6·53	7·28
	9	9·34	9·50	17·3	13·1	8·79	8·88	9·00	9·34
36D	1	2·71	3·25	12·0	5·9	2·26	2·79	2·16	2·61
	2	2·92	3·44	12·0	6·2	2·54	3·01	2·31	2·60
	4	5·68	6·07	7·6	6·5	4·90	5·23	5·32	5·24
	6	7·95	7·83	7·4	5·5	6·52	6·61	6·93	7·39
	9	10·41	10·63	7·4	6·1	8·94	8·98	9·16	9·53
108D	1	2·72	2·81	8·4	6·0	2·24	2·42	2·41	2·68
	2	2·93	3·10	7·3	5·9	2·40	2·67	2·51	2·86
	4	5·77	5·94	8·1	8·2	5·01	5·19	6·22	5·56
	6	8·72	8·10	6·3	6·6	7·29	6·92	7·25	8·31
	9	11·22	11·12	7·3	8·2	9·60	9·68	9·96	9·76

TABLE 2. Velocity distributions and comparison between gas velocity from flow rate measurements and from (void fraction × velocity) integration. d.c., drilled copper mixer.

probe technique for vertical flow through a 125 mm tube; they also found a very flat velocity distribution. For their case, the average void fraction was approaching 0·8, and gas-phase convection velocities were as high as 17·5 m s^{-1}.

Measuring the void and velocity distributions together can also indicate the reliability of the resistivity probe for measuring void fractions. By equating the local gas phase velocity u_g to the bubble convection velocity u_c, the average velocity of the gas phase $\langle u_g \rangle$ can be obtained from

$$\langle u_g \rangle = \langle \alpha u_g \rangle / \langle \alpha \rangle. \tag{26}$$

The value computed in this manner can be compared with the value given by flow measurements, Q_g and area A,

$$\langle u_g \rangle = Q_g / A. \tag{27}$$

The brackets $\langle\ \rangle$ denote area averaged values from integration.

The corresponding values of the velocity from (26) were determined by numerical integration: the values are listed in table 2. The values obtained from integration of the local flow properties are within about 10 % of the values obtained from flow rate measurements, and are generally lower. This can be explained partially by the fact that we expect the measured values of void fraction to be slightly low, because of possible deflexion of the smallest bubbles, and because of the minimum bubble resolution size of the probes. In all cases, the difference is less than 20 % of the value calculated from the overall gas flow rate, with only 4 of the total 30 runs showing a deviation greater than 10 %. For flow condition 2, the relative errors were large for the flow from both mixers at

36 diameters (– 15·8 % for drilled copper, – 10 % for nozzle); but they were in the opposite sense to that expected, as were the relative errors for flow condition 1 at this axial position. Flow condition 6, from the drilled copper mixer, also shows relatively large discrepancies in the calculated velocities; but this is a high void fraction condition, in which most of the gas seemed to be travelling in the form of slugs. However, it is likely that the air in the slugs was not travelling at the same speed as the air in the dispersed bubbles; the latter moved more slowly, because of the lower expected relative drift velocity.

Thus it was found that, for the two mixers known to give different void profiles, there were variations in the velocity profiles as well. There is no evidence to suggest a proportionate correspondence between void and velocity profiles, as suggested by Beattie (1972), especially at low flow rates, where there were no peaks in velocity profiles corresponding to those observed in the void profiles of figure 7. However, the velocity profiles tended to be flatter for these conditions. The results of most of the experiments show that it is possible to reconcile void and velocity profiles with the overall gas flow rate on average to within approximately 6 % for bubbly flow conditions, a slightly low estimate of gas volume flux usually occurring owing to deflexion of small bubbles.

Bubble size measurement

As indicated in the block diagram of the instrumentation (figure 3), a device was included to convert the void fluctuation signal to a signal of constant width pulses whose heights were proportional to the widths of the original pulses (i.e. a pulse height modulated signal was produced). Calibration of the pulse width to pulse height converter indicated a linear relation between input pulse width and output pulse height. The correlator/probability analyser was used to give a probability analysis of the voltage signal from the converter that gave the probability density function of bubble detection times. With the earlier assumption that all bubbles detected at a point have the average convection velocity, we can convert this into the probability density distribution of the chord lengths of detected bubbles, which is the function $\rho_3(x)$ referred to earlier.

In figure 9, a typical measured distribution is presented: one can see a peak in it at zero volts. This was due to the nature of the pulse height modulated signal, which was essentially a zero-voltage signal with intermittent pulses of very short duration (0·1 ms) in comparison with the spacing between pulses (usually around $10 \times 0{\cdot}1$ ms). A peak also occurred at the voltage representing zero pulse width, because of the finite width of the height modulated pulses. If the spacing between two of the pulses of the input signal was less than the output pulse width, the converter did not produce a pulse of the correct height proportional to the width of the first pulse; rather, it indicated a finite size pulse. For consistency, the contribution of these pulses to the distribution function was eliminated by joining points A and B of figure 9. This procedure undoubtedly introduces some uncertainties in the small size range, but for the purpose of this study, to compare different flows, this was not serious. In any case, as shown below in a discussion of mean diameters, and later by comparisons with measured autocorrelation func-

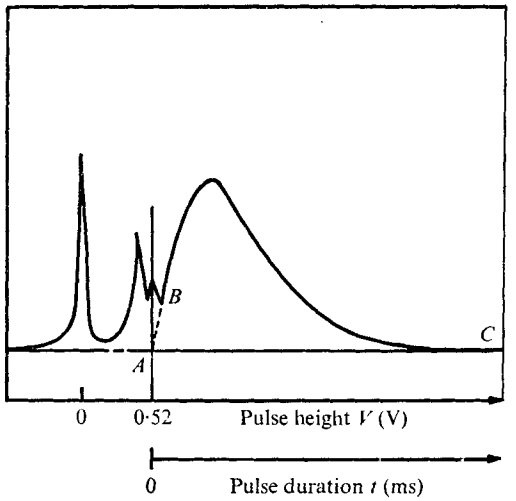

FIGURE 9. Distribution function of bubble detection periods (curve ABC), as determined from pulse height modulated signal.

tions, this approximation for the chord length curve does not introduce serious errors.

Simultaneous with void and velocity measurements, the pulse width distribution functions were recorded for four flow conditions. The distributions of the diameters of detected bubbles are most easily represented in terms of the cumulative probability distributions obtained from the measured chord-length distribution by (14). In figure 10, these distributions have been plotted to show the size distribution for flow condition 4 from both the drilled copper and nozzle mixers for development from position $8D$ to $108D$. Figure 11 shows the corresponding results for flow condition 9. It is clear that the two mixing conditions produced flows with different sized bubbles; but, as the flows developed, the bubbles from the drilled copper mixer broke up and became smaller, while the size of bubbles from the nozzle mixer increased, owing partly to bubble coalescence, and partly to the increased gas volume flow resulting from the pressure drop. The mean value of diameter $E(D)$ can be determined by

$$E(D) = \lim_{D\to\infty} \int_0^D D\rho_5(D)\,dD. \tag{28}$$

The determination of $\rho_5(D)$ by (13) requires differentiation, and consequently some scatter will result. From the discrete points of the distribution, the mean value was estimated by

$$E(D) = \frac{1}{N} \sum_{i=1}^{N} D_i \rho_5(D_i). \tag{29}$$

These values were tabulated below the relevant distributions. From the normalization of the distribution $\rho_6(D)$, which represents the proportionate contribution density to total voidage, we saw that the local gas volume flux q_g could be related to the mean bubble diameter and frequency, as in (21). For a locally homogeneous situation, on which this bubble size analysis depends, the local bubble flux is equal

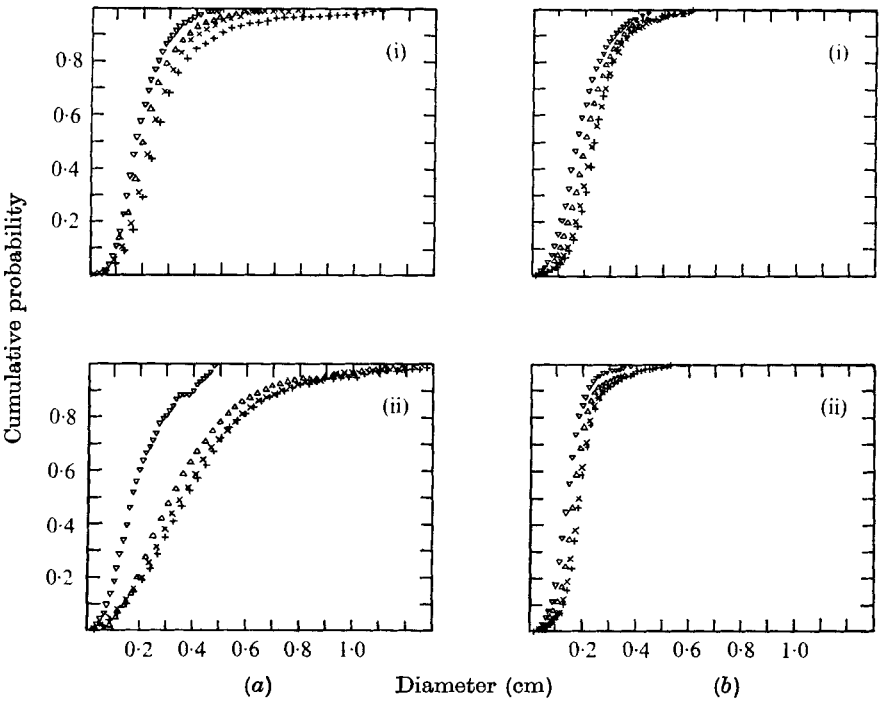

FIGURE 10. Bubble size distributions for flow condition 4. Mixers: (*a*) nozzle, (*b*) drilled copper. (i) 108*D*, (ii) 8*D*.

		(*a*)(i)		(*a*)(ii)		(*b*)(i)		(*b*)(ii)	
	r/*R*	*E*(*D*)	D_m	*E*(*D*)	D_m	*E*(*D*)	D_m	*E*(*D*)	D_m
+	0	0·26	0·22	0·41	0·28	0·24	0·20	0·20	0·17
×	0·4	0·25	0·20	0·40	0·28	0·24	0·20	0·19	0·17
△	0·7	0·22	0·18	0·36	0·25	0·21	0·17	0·18	0·15
▽	0·9	0·19	0·12	0·18	0·17	0·18	0·14	0·15	0·13

to the product of local void fraction and velocity, so that from (28) we can write

$$\frac{3\alpha u_g}{2N_d} = \int_0^\infty D\rho_5(D)\,dD. \tag{30}$$

This provides us with another means of estimating the mean bubble diameter. The values of $(3\alpha u_g)/(2N_d)$ were thus tabulated in the captions of figures 10 and 11 with the integrated estimates; they are labelled D_m and $E(D)$, respectively.

Agreement between these two estimates of mean diameter will depend on the reliability of the differentiation procedure for calculating $\rho_5(D)$, and on that of the overall technique for determining the distribution. It will also reflect the homogeneity of the flow structure. So we expect reasonable agreement when the experimental $P_5(D)$ curves of figures 10 and 11 are smooth, and where the bubble sizes cover only a narrow range, which is evidenced by the values tabulated in the captions of figures 10 and 11. Determination of the probability distribution $\rho_5(D)$ required differentiation, as in (13). Typical distributions are shown in

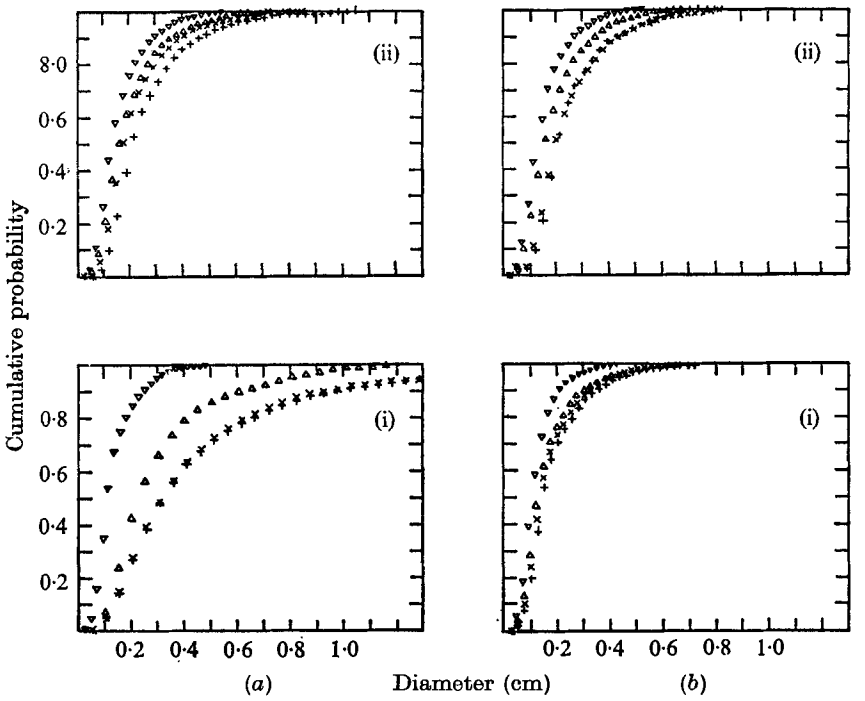

FIGURE 11. Bubble size distributions for flow condition 9. Mixers: (*a*) nozzle, (*b*) drilled copper. (i) 108*D*, (ii) 8*D*.

		(*a*)(i)		(*a*)(ii)		(*b*)(i)		(*b*)(ii)	
	r/R	$E(D)$	D_m	$E(D)$	D_m	$E(D)$	D_m	$E(D)$	D_m
+	0	0·26	0·26	0·46	0·42	0·25	0·21	0·19	0·19
×	0·4	0·22	0·23	0·45	0·38	0·24	0·20	0·17	0·17
△	0·7	0·20	0·18	0·30	0·26	0·19	0·17	0·16	0·16
▽	0·9	0·16	0·12	0·13	0·12	0·16	0·12	0·12	0·11

figure 12 for two axial locations. These curves were determined from a second-order numerical differentiation. To obtain these distribution functions for all flow conditions, some form of nonlinear regression would be necessary, but for the comparative purposes the cumulative distributions were sufficient and easily obtained.

The bubble size results provide strong evidence for the existence of a preferred or 'equilibrium' structure for these air–water mixtures, dependent only on the air and water flow rates. It is thus likely that we can make predictions about the properties of these 'equilibrium' structures. The break-up of bubbles rising under buoyant action has been discussed by Levich (1962). However, no consideration was given to the existence of a preferred bubble size under the action of strongly turbulent conduit flow of both phases, where the densities of the two phases are substantially different and the liquid phase is continuous.

In single-phase turbulent pipe flow, there is a continual production of energy due to shearing stresses, which results in fluctuation about the mean flow properties. The velocity fluctuations determine the turbulent kinetic energy within the

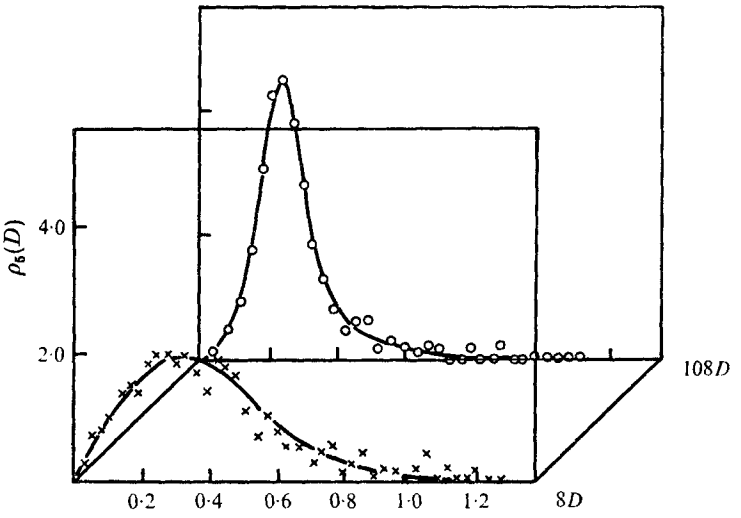

FIGURE 12. Axial development of the bubble diameter distribution functions for flow at the tube centre for flow condition 4.

flow, and provide the mechanisms for dissipation of the energy. It is now proposed that turbulent energy is similarly produced by shearing stresses in the continuous phase of a two-phase flow, but that the energy is contained in the mixture both as turbulent kinetic energy and also as energy of the interfacial structure. The action of turbulence produces a complex interfacial structure, in which the surface-tension forces (or stored energy) interact with the turbulent dynamic forces (or kinetic energy). A relatively simple estimate of the expected mean bubble size may be thus obtained by assuming that turbulent and surface-tension effects interact in such a way that the energies contained in the turbulent kinetic energy and in the surface energy of the resulting structure are equal. The energy associated with the surfaces of the bubbles for a given volume fraction will vary, depending on the size adopted by the bubbles. Small mean bubble sizes lead to a larger surface area than would large bubble sizes for a given volume fraction. At extremes of low or high void fraction, this energy would be relatively low. However, for moderate void fractions, an equilibrium between the forms of energy would be a reasonable physical postulate. The energy per unit volume is

$$E = \tfrac{1}{2}\rho_m q'^2 + \frac{6\sigma\alpha}{D} + \left(p + \frac{4\sigma}{D}\right) \ln\left(1 + \frac{4\sigma}{pD}\right). \tag{31}$$

ρ_m is the mixture density, q' the turbulent velocity fluctuation, σ the surface tension, α the void fraction, and D the mean bubble size. An estimate of the turbulent velocity fluctuations may be obtained by assuming that conditions are approximately the same as those in single-phase turbulent pipe flow. Davis (1974) showed that, for two-phase flow, friction factors similar to those for single-phase flows are obtained, basing normalization of data on mixture density and liquid-phase viscosity. It seems therefore that the assumption that the single-

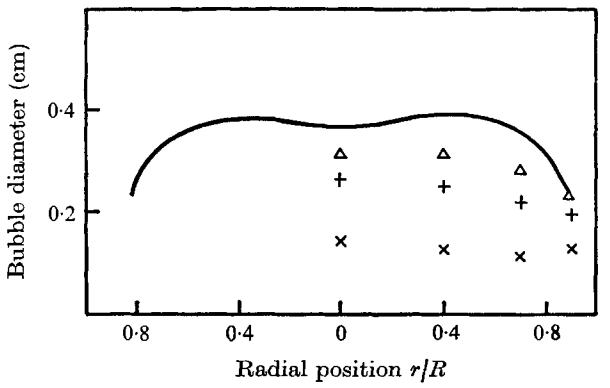

FIGURE 13. Comparison between predicted and measured bubble diameters for drilled copper mixer, flow condition 4 at $108D$. ——, estimated values for equipartition of energy. Mean value: △, from $\rho_6(D)$; +, from $\rho_5(D)$; ×, from $\rho(D)$.

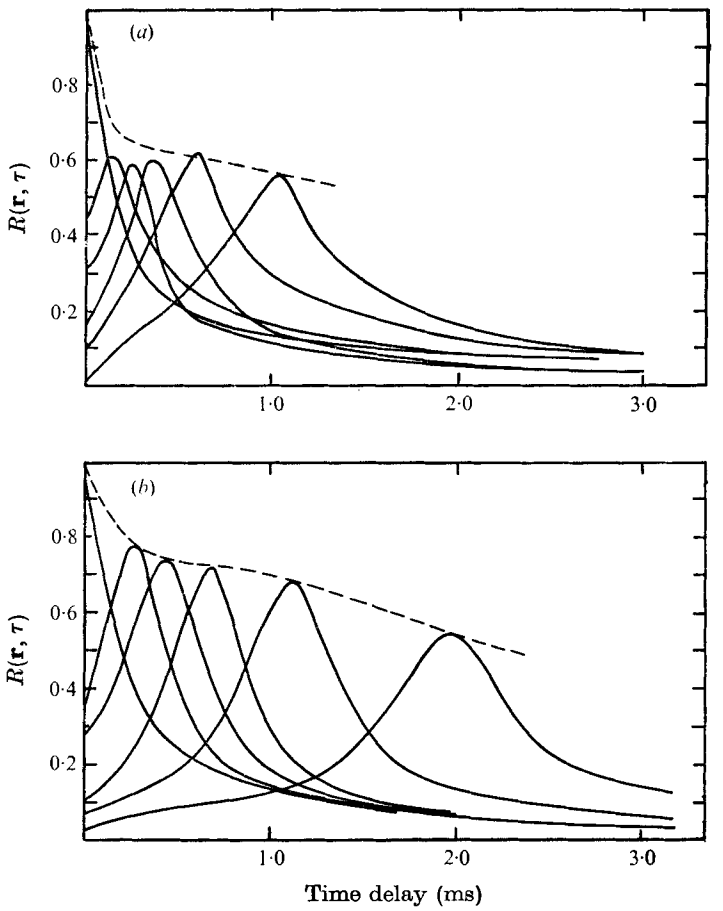

FIGURE 14. Space–time correlation functions at centre of pipe, for drilled copper mixer at $36D$. Flow condition: (*a*) 4, (*b*) 9. – – – –, estimation of moving-axis autocorrelation functions.

phase turbulent energy per unit volume is approximately representative for energy E will not be grossly in error. From the results of Laufer (1954), the average total single-phase turbulent kinetic energy per unit volume, over the pipe cross-section, is $0{\cdot}056\ \rho U_{\max}^2$; this is assumed equal to the energy per unit volume E. The pressure term in (31) is small, and the turbulent and interfacial terms are assumed to be equal. Thus, we may obtain an estimate of the mean bubble size. The result for one flow condition is shown in figure 13, together with experimental values from the distributions $\rho_6(D)$, $\rho_5(D)$ and $\rho(D)$. This result is typical of all the experimental data, with the estimated values being close to the $\rho_6(D)$ mean values, as would be expected, since this represents the mean size on the basis of contribution to total voidage. Over a total of sixteen experimental points in the more developed flow conditions the average error was an over-estimate of size by 13 %.

Signal correlation measurements

For two different flow rates, the correlation function $R(\mathbf{r}, \tau)$, defined by (22), has been measured for the position vector $\mathbf{r}$ both parallel to and perpendicular to the flow directions, as illustrated in figure 14. For flow condition 4, the curves are similar to the equivalent correlation function obtained for single-phase turbulence measurements by Favre (1965) and Comte-Bellot & Corrsin (1971), with the function for each probe separation showing a maximum value at a time delay equal to the mean transport time of the gas phase. As might be expected, the value of this maximum correlation coefficient decreases with increasing probe separation, the dotted line drawn through these maxima in figure 14 representing the moving-axis autocorrelation function. For condition 9, the maximum correlation coefficients for the three smallest separation distances are most likely low, owing to the interference of the front probe in the flow which was detected by the second probe. For these smaller separation distances, this effect did not appear to be as great for condition 4, which could be related to the fact that for condition 4 the void fraction is lower. The difficulties in measuring correlations with one probe downstream of another are well known; in the two-phase mixture, it was observed that a bubble often attached itself to the front probe and remained within the wake, so that it was necessary to have the rear probe displaced a small distance laterally. During the experiments, the alignment was set at low void fraction conditions, so that it could be seen that the attached bubble did not interfere with the second probe. The probe was then maintained in that position, since for the conditions tested it was not always possible to see the probe. For condition 9 it may thus have been this wake, or bubble, attachment that caused the relatively low correlation coefficients for the small axial separations. Comte-Bellot & Corrsin (1971) discussed the wake problem with regard to turbulence measurements. They proposed that it is best to measure the correlation function for several lateral displacements (Δy) outside the wake, and then to extrapolate the values to the limit $\Delta y = 0$. It appears that this procedure also obtains more accurate correlation functions in two-phase situations. Although this attached wake has had some effect on the measured correlation functions, the moving-axis autocorrelation functions, estimated by the dashed lines in figure 14, serve to

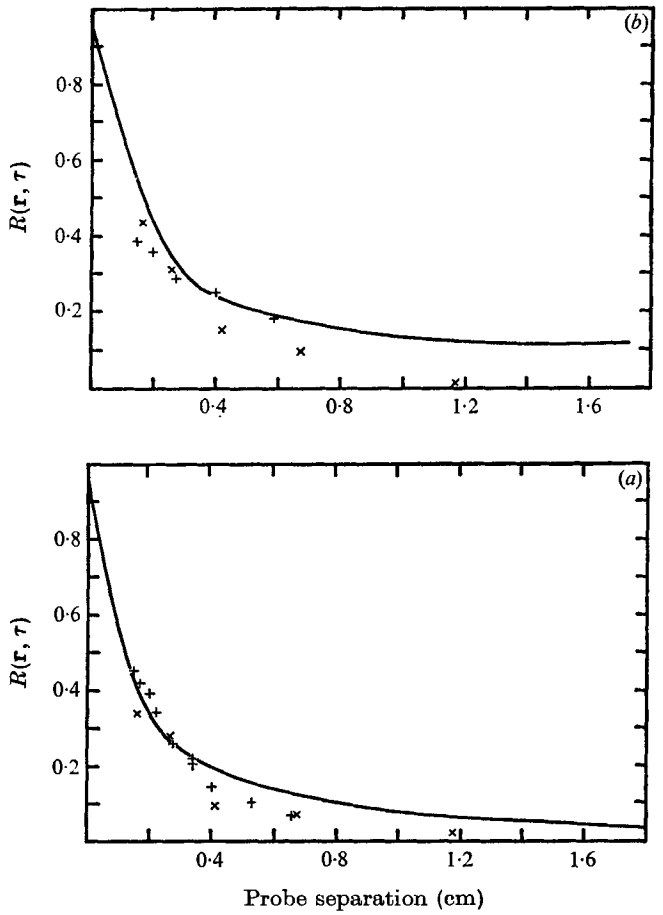

FIGURE 15. Spatial correlation $R(\mathbf{r}, 0)$ and autocorrelation function $R(0, \tau)$ for flow at pipe centre $36D$ from drilled copper mixer. ——, $R(0, \tau)$ with $r = u_c\tau$. +, $\mathbf{r} = y$, lateral; ×, $\mathbf{r} = x$, axial. (*a*) Flow condition 4. (*b*) Flow condition 9.

compare the rate of reorganization of the flow structure for the one flow rate with that for the other. The structure of the flow for condition 9 appears to change much more quickly than that for condition 4, as indicated by the faster decline in the moving-axis autocorrelation function. This would be due to the fact that the mixture velocity for condition 9 is much higher than that for condition 4, as is the turbulence intensity. However, for separations greater than those measured here, this will not necessarily be true, since the flow in condition 9 contained intermittent gas slugs and might have a higher correlation for larger separation.

The correlation functions $R(\mathbf{r}, 0)$ can be used to assess the homogeneity of the flow structure, by comparing the values in the lateral and longitudinal directions. Lateral correlation functions were obtained for two flow conditions, by placing one probe in the centre of the tube and traversing a second probe towards it. The values of these correlations are compared in figure 15. There seems to be a good correspondence between the lateral and longitudinal values. If we assume that

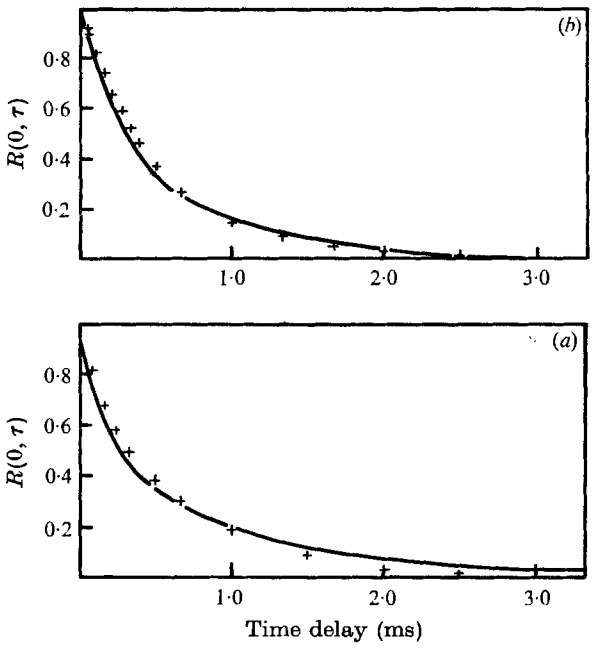

FIGURE 16. Comparison of autocorrelation functions from direct measurement and conversion from pulse period probability distributions, drilled copper mixer at 8*D*. ——, measured autocorrelation function; +, value from bubble period measurements. (*a*) Flow condition 9. (*b*) Flow condition 4.

velocity and displacement are related by $x = u_c\tau$, then the autocorrelation and the spatial correlation functions may be equated. If the flow is homogeneous, the autocorrelation should also correspond to the lateral spatial correlation coefficient through the convection velocity. Autocorrelation functions are presented in figure 15, and it appears that the correlation coefficients fall somewhat below the autocorrelation function for larger separation distances. The lateral and longitudinal spatial correlations are close to the autocorrelation function for smaller separation distances.

Equations (23) and (24) give a relation between the autocorrelation function and the pulse time probability function $p(\tau)$, from which the bubble diameter distributions were derived. Using these relations, the autocorrelation function can be calculated numerically from the measurements of the pulse durations. Direct comparison of this calculated autocorrelation function with the function measured by the correlator/probability analyser indicates the extent of correlation between individual pulses. (Equation (23) was derived on the assumption that there is no correlation between pulses.) Again, the comparison gives some indication of the reliability of the pulse width to pulse height conversion apparatus. Comparison of the curves with calculated points shows them to be very close for small time delays, with only slight discrepancies arising at relatively long time delays (figure 16). For both flow conditions shown, the measured autocorrelation functions are steeper near zero time delay, which is probably a result of the uncertainties in the pulse width to pulse height conversion for small pulse

durations, and the inability of the system to handle pulses shorter than a certain minimum duration.

6. Discussion of results

The experiments reported in this paper were carried out for nine standard flow conditions (table 1). In § 1 several investigations were discussed that measured void and velocity profiles in vertical flow, most of the results being for flow conditions with low mixture velocities approximately corresponding to conditions 1–3 of table 1. Different types of inlet conditions were used for the various studies, and showed that low flow rate conditions are the ones that appear to depend mostly on inlet conditions. However, for flow condition 1 of this study, most inlet conditions gave void profiles with local maxima near the tube wall, except the drilled copper mixer, which gave a maximum void fraction at the centre. When a screen was located in the mixer, the void profile at $8D$ was noticeably flatter, with slight local maxima away from the tube centre; and by $108D$ the shape was the same as that given by the other mixers. This suggests that this type of phase distribution, with maxima near the tube wall, is a stable condition for such low velocities (below about $3\,\mathrm{m\,s^{-1}}$). It has previously been thought, as suggested by Malnes (1966) and Neal & Bankoff (1963), that these local maxima near the tube wall were purely a function of inlet conditions, whereas these experiments showed that this is not necessarily so.

More generally, in flows where mixtures closely approached conditions independent of inlet mixing, void profiles showed a local minimum at the tube centre. This was so for all flow conditions, except the high void fraction cases (3, 6 and 9 of table 1). Flow condition 2 appeared to be unusual, in that the void distribution seemed to depend upon inlet conditions even at $108D$ from the mixer. For this condition with the drilled copper mixer, slugs were observed to be present in the flow at $108D$.

The apparent convergence of the structure of the flows from the different mixers was evidenced by the void profiles, the velocity distribution and especially by the bubble size distributions, which clearly indicated this trend even for flow condition 2. That is, for the nozzle mixer, bubbles entered the test section apparently smaller than their equilibrium size, while, for the drilled copper mixer, they were significantly larger. As the flow developed, these size differences diminished, so that at $108D$ there was very little difference in the size of bubbles from the different mixers.

Sample correlation data was obtained for two flow conditions, to verify the reliability of the instrumentation for the bubble size measurements, to allow determination of mean transport velocities, and to assess the rate of change of the flow structure and the flow homogeneity. In figures 12 and 13, the rate of decay of the flow structure was represented by the moving-axis autocorrelation function. Under flow condition 4, after the flow had travelled for 2 ms (which corresponded to a distance of approximately 1·2 cm), the correlation coefficient was still above 0·5, and was decreasing very slowly. The structural lifetime, at which the correlation decreased to $1/e$, would on the basis of these results be

approximately 4 ms, or approximately 2·4 cm. These curves were recorded with the probe at $36D$, where the size of the bubbles was between the value at $8D$ (0·25 cm) and at $108D$ (0·41 cm). Under flow condition 9, the moving-axis autocorrelation showed a much sharper initial decrease than for flow condition 4, but then decreased more slowly with regard to the time axis. This is consistent with the observation of slugs of air in the flow.

7. Concluding remarks

The indications of this experimental study are that air–water mixture flows tend to develop towards a common equilibrium structure, independent of the inlet mixing method. This was evidenced by the bubble size distribution, the velocity profiles, which appeared to be grouped around a $\frac{1}{7}$ power law distribution, and by the void profiles, which for dispersed (or bubbly) flows generally have characteristic local minima at the centre of the pipe. Application of correlation procedures common in turbulence investigations provided a means of assessing the rate of reorganization of the flow structure and the homogeneity of the flow.

Estimates of bubble size based on equipartition of energy between turbulent motion and surface-tension energy of the surface structure give a good indication of the mean bubble size occurring in practice. The measuring techniques employed appeared to be reliable, in that the measured gas volume flux rate was consistent with the known mass flow, and that the measured bubble size distributions and signal autocorrelations were consistent.

REFERENCES

Alves, G. E. 1954 *Chem. Eng. Prog.* **50**, 449–456.

Amiantov, I. N. & Tikhonov, V. I. 1965 *Nonlinear Transformations of Stochastic Process* (ed. Kuznetsov *et al.*). Pergamon.

Beattie, D. R. H. 1972 *Nuclear Engng & Design*, **21**, 46–64.

Champagne, F. H., Harris, V. G. & Corrsin, S. 1970 *J. Fluid Mech.* **41**, 81–139.

Comte-Bellot, G. & Corrsin, S. 1971 *J. Fluid Mech.* **48**, 273–337.

Davis, M. R. 1974 *J. Fluid Engng*, **2**, 173–179.

Favre, A. J. 1965 *J. Appl. Mech.* **32**, 241–257.

Griffith, P. & Wallis, G. B. 1961 *J. Heat Transfer*, **83**, 307–320.

Herringe, R. A. 1973 Ph.D. thesis, University of New South Wales.

Herringe, R. A. & Davis, M. R. 1974 *J. Phys.* E **7**, 807–812.

Hewitt, G. F. & Bouré, J. A. 1973 *Int. J. Multiphase Flow*, **1**, 139–172.

Lackmé, C. 1967 *C.E.N. Grenoble Rep. CEA-R* 3203.

Laufer, J. 1954 *N.A.C.A. Rep.* no. 1174.

Lecroart, H. & Porte, R. 1971 *Proc. Int. Symp. on Two-Phase Systems*. Technion Haifa, paper 3–11.

Levich, V. G. 1962 *Physicochemical Hydrodynamics*. Prentice Hall.

Malnes, D. 1966 *Institutt for Alomenergi, Kjeller, Norway Rep.* no. 110.

Miller, N. & Mitchie, R. E. 1970 *J. British Nucl. Eng. Soc.* **9**, 94–100.

Nassos, G. P. 1963 *Argonne National Laboratory Rep.* no. 6738.

Neal, L. G. & Bankoff, S. G. 1963 *A.I.Ch.E. J.* **9**, 490–494.

Oshinowo, O. & Charles, O. 1974 *Can. J. Chem. Engng*, **52**, 25–35.

Taylor, G. I. 1938 *Proc. Roy. Soc.* A **164**, 476–490.